

Neutral hydrogen density profiles derived from geocoronal imaging

N. Østgaard,¹ S. B. Mende,¹ H. U. Frey,¹ G. R. Gladstone,² and H. Lauche³

Received 24 October 2002; revised 10 January 2003; accepted 25 February 2003; published 23 July 2003.

[1] Measurements of the Lyman α column brightness by the Geocoronal Imager (GEO), part of the FUV imaging system on board the IMAGE satellite, have been used to derive an empirical model of the neutral hydrogen density distribution at high altitudes ($>3.5 R_E$ geocentric distance) on the night-side of the Earth. The model presented is an effort to provide the density profiles needed to analyze the energetic neutral atom imaging data at ring current altitudes and above. The variable solar Lyman α flux is obtained from the UARS/SOLSTICE measurements and the scattered solar Lyman α emissions from interplanetary hydrogen are obtained from a model. Assuming that the exosphere at high altitudes ($>3.5 R_E$ geocentric distance) can be considered as an optical thin medium and that the hydrogen density profile can be expressed as a double exponential we show that the Lyman α column brightness can be converted to hydrogen density profiles. The hydrogen density above $5 R_E$ is found to be slightly higher for large solar zenith angles than for 90° solar zenith angle. The hydrogen density shows temporal variations which are not controlled by any solar quantity or geomagnetic parameter alone. Our Lyman α profiles and derived hydrogen density profiles are close to what was observed by Dynamics Explorer 1 [Rairden *et al.*, 1986]. Above $8 R_E$ we find higher densities than they did for all solar zenith angles $>90^\circ$. We do not find any evidence of depletion due to charge exchange with solar wind protons outside the magnetopause. Our results are only valid above $3.5 R_E$.

INDEX TERMS: 0343 Atmospheric Composition and Structure: Planetary atmospheres (5405, 5407, 5409, 5704, 5705, 5707); 0310 Atmospheric Composition and Structure: Airglow and aurora; 0350 Atmospheric Composition and Structure: Pressure, density, and temperature; 0360 Atmospheric Composition and Structure: Transmission and scattering of radiation; **KEYWORDS:** Neutral hydrogen density, geocorona, imaging, Earth's atmosphere, exosphere

Citation: Østgaard, N., S. B. Mende, H. U. Frey, G. R. Gladstone, and H. Lauche, Neutral hydrogen density profiles derived from geocoronal imaging, *J. Geophys. Res.*, 108(A7), 1300, doi:10.1029/2002JA009749, 2003.

1. Introduction

[2] The geocorona is produced when solar Lyman α radiation is resonance scattered by exospheric neutral hydrogen. Since rocket-borne experiments [e.g., Kupperian *et al.*, 1959; Donahue, 1966] provided the first measurements of the geocoronal Lyman α in the late 1950s, efforts have been made to model the neutral density profiles [Chamberlain, 1963; Tinsley *et al.*, 1986; Bishop, 1991; Hodges, 1994] and to predict the Lyman α intensities that can be observed from space [Anderson and Hord, 1977; Anderson *et al.*, 1987; Bishop, 1999].

[3] Owing to the analytical model developed by Chamberlain [1963], which has been widely accepted, the exosphere comprises three different neutral hydrogen pop-

ulations given three boundary conditions. This model assumes an exobase (~ 500 km), above which the collisions cease to be important, and an upper level ($2.5\text{--}3.5 R_E$) below which collisions are rare but can scatter particles into closed orbits. The third assumption is that no particles can enter the exosphere from infinity. With these boundary conditions the model describes the exosphere to be populated by three different particle populations. Ballistic particles are those that rise from the exobase with velocities less than escaping velocities and then fall back. Escaping particles leave the exobase and are lost from the exosphere. Satellite particles are defined as particles that are scattered into closed orbits. The upper level of rare collisions defines the upper bound for the perigee of satellite particles. According to this model there will be two density regimes above the exobase. Ballistic particles will dominate at low altitudes, but as the density of these particles rapidly falls off toward higher altitudes the satellite particles will dominate above the level of rare collisions, forming a tail in the density profile. The transition between the ballistic dominated and the satellite dominated regimes depends on the exobase temperature and where the upper level of rare collisions is defined. Escaping particles will be present at

¹Space Sciences Laboratory, University of California, Berkeley, California, USA.

²Southwest Research Institute, San Antonio, Texas, USA.

³Max Planck Institute for Aeronomy, Katlenburg-Lindau, Germany.

all altitudes and at very high altitudes these particles will be the only population left.

[4] *Tinsley et al.* [1986] and *Bishop* [1991] suggested some improvements to the Chamberlain model by taking into account that collisions between hydrogen atoms and ionospheric-plasmaspheric ions may be more effective in establishing the satellite hydrogen population than only considering collisions between neutrals. They also included a “radiation pressure” acting on the satellite population to model the asymmetric exosphere with slightly higher densities at high altitudes in the anti-sun-ward direction, the so-called geotail. The model presented by *Tinsley et al.* [1986] shows a significant geotail above $4 R_E$ and *Bishop* [1985] estimated an excess in column density of $2 \cdot 10^{11}$ [atoms cm^{-2}] for the geotail compared to the day-side column density. The model developed by *Hodges* [1994] also included both the neutral-neutral and the ion-neutral interaction processes and examined seasonal and solar cycle effects on the exospheric density. For solstice and $F10.7 = 180$, which corresponds to average solar maximum conditions, his result is close to *Tinsley et al.* [1986] below $4 R_E$ geocentric distance, but is a factor of ~ 2 lower at higher altitudes. A comprehensive model to estimate the Lyman α column brightness as measured at any point in space has been developed by *Bishop* [1999]. This model uses the hydrogen density profiles (at low altitude) from the MSIS-90 [*Hedin*, 1991] extended to exospheric altitudes via the analytical model by *Bishop* [1991]. The algorithm developed by *Anderson and Hord* [1977] and *Anderson et al.* [1987] is used to model the transport of photons. The actual solar Lyman α flux and background subtraction has to be specified by the user. Comparisons with earlier data of Earth’s limb profile [*Anderson et al.*, 1987] and geocorona [*Rairden et al.*, 1986] show that this model replicates the data fairly well, given the assumptions about solar Lyman α fluxes and calibration used in these studies [*Rairden et al.*, 1986; *Anderson et al.*, 1987].

[5] *Rairden et al.* [1986] used the geocoronal measurements from Dynamics Explorer 1 (DE 1) combined with the Chamberlain [1963] model and numerical solutions of the radiative transfer equations to develop a hydrogen density model at high altitudes. Although this model has been widely used in the analysis of ring current and ENA generation rates [see e.g., *Kistler et al.*, 1989; *Fok et al.*, 1995] it has been suggested that their hydrogen densities might have been overestimated as they used too low solar Lyman α fluxes [*Woods and Rottman*, 1997]. *Rairden et al.* [1986] found evidence in their data for the existence of a geotail, a feature which was first reported by *Thomas and Bohlin* [1972]. On the other hand, they did not find the satellite population to be depleted due to charge exchange with solar wind protons at high altitudes as severely as earlier investigations had suggested [e.g., *Wallace et al.*, 1970; *Bertaux and Blamont*, 1973]. In addition to providing a comprehensive examination of high altitude geocorona and a hydrogen density model, *Rairden et al.* [1986] also give a review of geocoronal observations prior to 1986. Except for limb-observations [*Anderson et al.*, 1987] and a report on one day of Lyman α zenithal observations by the Spacelab-1 mission [*Bertaux et al.*, 1989] there has been no comprehensive measurements to examine the Earth’s geocorona over the last two decades.

[6] In this paper we present hydrogen density profiles derived from measurements of the Lyman α (121.6 nm) column brightness provided by the GEO instrument [*Mende et al.*, 2000] flown on the Imager for Magnetopause-to-Aurora Global Exploration (IMAGE) satellite. Three other instruments on board the IMAGE satellite, HENA, MENA and LENA, are imaging the energetic neutral atoms (ENA) which are produced by charge exchange between energetic magnetospheric ions and the cold neutral hydrogen background. In order to convert the measurements of ENA to magnetospheric ion distributions, information about the neutral hydrogen density distribution at high altitudes ($>3.5 R_E$ geocentric distance) is needed. The results presented in this paper is an effort to provide such density profiles. As we are only interested in the densities at high altitudes ($>3.5 R_E$ geocentric distance) we can assume that the medium is optical thin. Under such an assumption we show that the Lyman α column brightness can be converted to hydrogen density profiles. To study the hydrogen density profiles at lower altitudes where the medium is not optical thin a more complex approach including a complete radiative transfer analysis [see e.g., *Tinsley et al.*, 1986; *Hodges*, 1994; *Bishop*, 1999] must be applied. The paper is organized as follows. In Section 2 we describe the instrument, the solar Lyman α variability, the temporally and spatially varying background of scattered solar Lyman α from interplanetary hydrogen and explain how the instrument is calibrated. In Section 3 we explain how the hydrogen density profiles can be derived from profiles of Lyman α column brightness assuming that the exosphere $>3.5 R_E$ can be considered as an optical thin medium. In Section 4 we explain the various corrections that have been applied to the data. In Section 5 we present the results based on 338 days of data between June 28, 2000 and June 22, 2001. In the two last sections (6 and 7) the results are discussed and summarized.

2. Instrumentation and Data Processing

2.1. Instrument Description

[7] The GEO instrument [*Mende et al.*, 2000] is part of the Far Ultraviolet (FUV) Imaging system flown on the IMAGE satellite and is designed to measure the column brightness of the geocoronal Lyman α . The instrument contains three photo-meters looking at 0° and $\pm 30^\circ$ relative to the spacecraft spin plane, each with a field of view (FOV) of 1° . The spin axis is nominally perpendicular to the orbital plane. The satellite was launched into an elliptical orbit with apogee (perigee) altitude of $\sim 7 R_E$ (1000 km). Owing to the Earth’s motion around the Sun the three sensors scan through different solar zenith angles and local times during the mission. Solar zenith angle is defined as the angle between the Sun-Earth line and local zenith, denoted φ_{SC} in Figure A1 in appendix A. The lines of sight for the upper and lower sensors form cones in space while the middle sensor lines of sight form a great circle. The photo-meters are sensitive to emissions from 110–140 nm (see quantum efficiency in *Mende et al.* [2000, Figure 22]), with a peak sensitivity around the Lyman α emission line at 121.6 nm. As long as the line of sight is not toward the Earth where atomic Oxygen emission at 130.4 nm is significant, our measurements contain only the scattered solar Lyman α

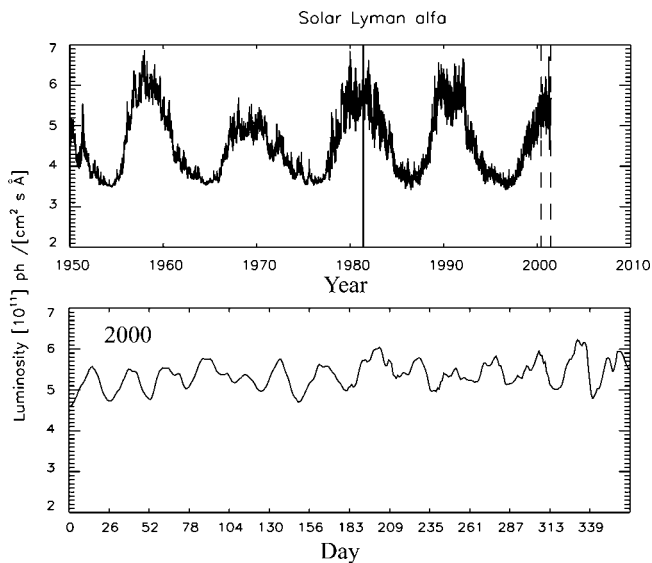


Figure 1. Variability of the Solar Lyman α flux. Solid line indicates when the data used by Rairden *et al.* [1986] were sampled and dashed lines show the time interval examined in this study.

emission from the geocorona and the interplanetary medium. In addition to the nominal FOV of 1° there is an off-axis component from $\pm 90^\circ$. This means that the photometers will be contaminated by solar Lyman α whenever the Sun is within approximately $\pm 90^\circ$. In order to avoid this contamination we have disregarded all data when the Sun is within $\pm 90^\circ$. It also means that there is an off-axis component in our measurement that has to be subtracted, as will be discussed below (subsection 2.4).

2.2. Variability of Solar Lyman α Flux

[8] The solar Lyman α flux, which is the source for the geocorona, is a variable quantity reflecting both the 27 day solar rotation and the 11-year solar cycle. In Figure 1 we show the variability on both scales based on the composite data set provided by Woods *et al.* [2000]. The values are based on direct measurements from several satellites. Owing to the better photometric accuracy of the Solar-Stellar Irradiance Comparison Experiment on board the Upper Atmosphere Research Satellite (UARS/SOLSTICE) all the other measurements were scaled to match the solar Lyman α flux measured by UARS/SOLSTICE [Woods *et al.*, 2000]. The $1-\sigma$ uncertainty was estimated to be $\pm 10\%$ for the long-term data set and $\pm 5\%$ for the UARS/SOLSTICE measurements. From solar minimum to solar maximum the fluxes vary by a factor of 1.5 on average up to 2.1 (maximum) while the variability over the 27 day cycle is $13\% \pm 7\%$ based on the direct measurements [Woods *et al.*, 2000]. Daily averages of the solar Lyman α fluxes from the direct measurements from UARS/SOLSTICE were available for the time interval examined in this paper (June 28, 2000–June 22, 2001). Since the geocorona responds instantaneously to any changes in the solar Lyman α flux, variations on a shorter timescale would be important. To examine such variations we have examined He II 30.4 nm emission measured by the Solar Extreme Ultraviolet Monitor (SEM) on board the SOHO satellite with a 15 s resolution. Although the He II 30.4 nm

emission is thought to vary about a factor of 1.2 more than the solar Lyman α these emissions can be used as a proxy for the variability of the solar Lyman α flux (T. Woods, personal communication, 2002). We found that the flux of He II 30.4 nm emissions usually only show the slow variations from day to day. Larger variations ($\sim 10\%$) are rare and recover in less than 30 min. This is consistent with shorter timescale variations of the solar Lyman α as measured by UARS/SOLSTICE. During solar flares the solar Lyman flux may increase rapidly by some percent and recovers in about 15 minutes, but typically the hourly variation is $< 1\%$ (G. Rottman, personal communication, 2002). Therefore we expect differences smaller than the $1-\sigma$ uncertainty in the daily average and will use the daily average as the line-integrated solar Lyman flux (ph/[cm²s]) measured by UARS/SOLSTICE. However, the relevant quantity in Lyman alpha atmospheric and interplanetary scattering is the line-center fluxes (ph/[cm²s Å]), which is assumed to be about 0.9 times the line-integrated flux [Pryor *et al.*, 1998a]. We have therefore adjusted the UARS/SOLSTICE measurements by a factor of 0.9 to obtain the line-center flux to be used in our calculations.

2.3. Background of Scattered Solar Lyman α Emissions

[9] Solar Lyman emissions scattered by interplanetary and local interstellar hydrogen constitute a background varying both in space and time. Daily maps of the spatial distribution of this background have been modeled by Pryor *et al.* [1996, 1998a, 1998b]. These maps are based on different measurements of the interplanetary Lyman emissions as well as other wavelengths that can be used as proxy for the Lyman fluxes. In Figure 2 we show the background from day 197 in 2000 as well as the look directions of the three sensors. The maximum (230°E , 0°N) is seen where the interstellar hydrogen flows into the heliosphere. The minimum (80°E , 10°S) is thought to be the result of charge exchange between the interstellar hydrogen and the solar wind protons and photo-ionization creating a cavity of hydrogen in the downwind direction [Pryor *et al.*, 1996, 1998a, 1998b]. The temporal variation of the background is due to different processes. It varies as the solar Lyman α varies with solar cycle (11 year) and solar rotation (27 days). It also changes because the interplanetary hydrogen density itself is affected by the solar wind changes and solar Lyman α pressure on the atoms. Typical model results for the background during 2000 and 2001 show a minimum of 0.27–0.36 kilo-Rayleigh [kR] and a maximum of 1.2–1.5 kR. As these maps depend on different Lyman measurements, the accuracy of the model is limited by large calibration discrepancies (factor of 2 or more) between the different instruments at Lyman α [Pryor *et al.*, 1998a]. This unknown uncertainty may represent a systematic error in our results as the background intensity is comparable to the geocoronal intensity at high altitudes and will be discussed.

2.4. Calibration

[10] The calibration of the detectors was based on the known luminosity of stars, and the quantum efficiency (QE) and the point spread function (PSF) of the detector. Only the upper and middle sensors scan in directions of known stars and due to the small FOV of only 1° , we do not know if the

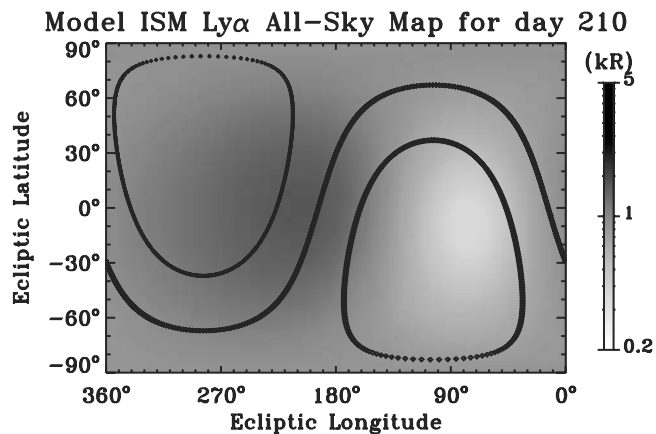


Figure 2. All-sky maps of scattered Lyman α from interplanetary hydrogen based on a model by Pryor *et al.* [1996, 1998a, 1998b]. Center line of sight for the three detectors are also shown. The circular shaped scan to the right (left) is the upper (lower) sensor line of sight, while the middle sensor makes a S-shaped scan.

peak of the star luminosity is in the center of our FOV. However, by sampling star measurements for many days we obtained a distribution of peaks showing the star passage through the 1° FOV. The maximum of this distribution can then be interpreted to be when the star is centered within the 1° FOV of the detector and represents the observed count rate of the star. Figure 3 shows the distributions of 28600 measurements of β Crucis and 15251 measurements of γ Cassiopeia when interplanetary background and geocorona are subtracted. These measurements were sampled during 62 days from March 9–May 10, 2001. The uncertainty of the observed star count rates should be no more than 10%. The measured spectra of β Crucis, β Muscae and γ Cassiopeia, obtained from the International Ultraviolet Explorer (IUE), were folded through the GEO band pass [see Mende *et al.*, 2000, Figure 22] to get the predicted count rates. The ratio of observed to predicted counts of these stars gives us the corrected QE at 121.6 nm for the middle sensor with an estimated $1\text{-}\sigma$ uncertainty of $\pm 10\text{--}15\%$. Finally, to estimate the count rates per 1 kR from a uniform diffuse source of Lyman α we use the QE at 121.6 nm and the cylindrical symmetric point spread function (PSF) shown in Figure 4. The PSF is based on laboratory calibration with 632.8 nm light beam from a helium-neon (HeNe) laser and a theoretical scattering analysis of Lyman α in the GEO tubes. The counts per kR for the middle sensor was found to be 240 and the on-axis component was found to be $40\% \pm 8\%$, which gives us the on-axis counts per kR = 96 with a $1\text{-}\sigma$ uncertainty of $\pm 25\%$. As will be discussed in section 4 and shown in section 6 both the anisotropic cross section and the existence of the geotail count for a slightly non-uniform source, which could lead to a different on-axis component than given a uniform source. Fortunately, the off-axis contribution is mainly from within 20° (relative to the center-line). The variations due to the an isotropic cross section and the geotail are therefore too small in the 20° cone around the center-line to affect the on- and off-axis contribution significantly. Model results with such an

isotropic sources (not shown) indicate variations of the on-axis component of only 1–2%, which is well within the uncertainty of our estimate of the on-axis component.

3. Method to Derive Hydrogen Density Profiles From Lyman α Brightness

[11] We consider the corrected and background subtracted on-axis component of the Lyman α column brightness, $M_C(r)$ [kR], measured when looking toward local zenith as a function of geocentric distance. The correction scheme will be explained in section 4, appendices A and B, and is given by equation 11. This approach is based on the assumption of an optical thin medium and is therefore only valid at high altitudes. Following Anderson and Hord [1977] we first define the optical depth, τ , along a line of sight

$$\tau = \sigma \cdot N \quad (1)$$

where σ [cm^2] is the line center cross section, taken to be $5.9 \cdot 10^{-12} \cdot 1050^{-1/2}$ [Bishop, 1999], where 1050 [K] is a reference temperature [Rairden *et al.*, 1986] and N [cm^{-2}] is the column density of neutral hydrogen along an optical path in the medium. We define the medium to be optical thin where $\tau \leq 0.1$ [Anderson and Hord, 1977], which means that more than 90% of the photons will only be subject to single scattering. As τ depends on the hydrogen density profile we have calculated the geocentric distance

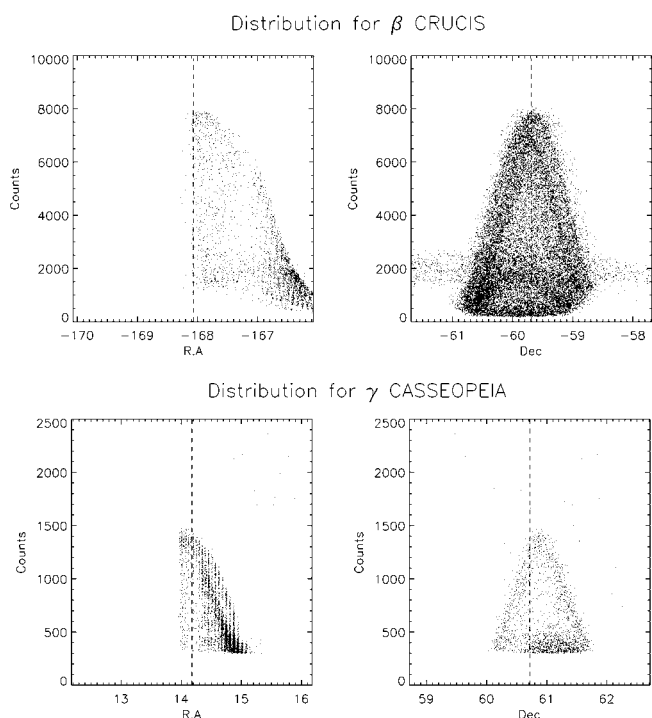


Figure 3. Distribution in right ascension (left) and declination (right) of β Crucis (26800 data points) and γ Cassiopeia (15251 data points) measured by the middle sensor during 62 days. Geocorona and background are subtracted. The true positions of the stars are indicated with dashed lines.

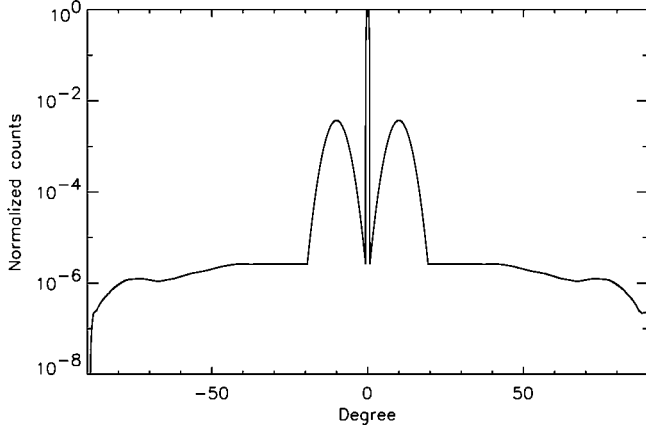


Figure 4. The normalized cylindrical symmetric point spread function for the GEO sensors based on laboratory calibration with 632.8 nm light beam from a HeNe laser and a theoretical scattering analysis of Lyman α in the GEO tubes.

where $\tau = 0.1$ using the density estimates from *Rairden et al.* [1986], *Tinsley et al.* [1986] as well as the results from this study. The values are listed in Table 1.

[12] On the basis of these values we define the geocentric distance where the medium becomes optical thin to be not higher than $\sim 3.5 R_E$. Under the assumption of an optical thin medium (i.e., only single scattering is assumed) the emission rate, $4\pi I(r)$, will be proportional to the flux of incident photons and the optical depth along a line of sight. Further following *Anderson and Hord* [1977], in units of effective solar flux, F , the emission rate can be expressed as

$$M_C(r) = 4\pi I(r) = \sigma \cdot F \cdot N(r) \quad (2)$$

where $4\pi I(r)$ and F can be expressed in kR. An apparent emission rate $4\pi I = 1$ kR is equivalent to an intensity $I = 10^9$ photons $[4\pi \cdot \text{cm}^2 \cdot \text{s} \cdot \text{sr}]^{-1}$. The effective solar flux has the form

$$F = \pi f \cdot \Delta\gamma_D \sqrt{\pi} \quad (3)$$

where πf is the line-center solar flux of photons $[\text{cm}^2 \cdot \text{s} \cdot \text{\AA}]^{-1}$ (which is taken to be 0.9 times the line-integrated flux obtained from UARS/SOLSTICE, see Section 2.2) and $\Delta\gamma_D$ is the Doppler width, taken to be $5.21 \cdot 10^{-4} \cdot \sqrt{1050}$ [Å] [*Bishop*, 1999], where 1050 [K] is the reference temperature taken from *Rairden et al.* [1986]. Notice that the Lyman α column brightness, $M_C(r)$, refers to the corrected Lyman α column brightness given by equation 11 and described in Section 4, appendices A and B. An expression for the column density of neutral hydrogen, $N(r)$, is obtain by assuming that the volume density altitude profile, $n(r)$, can be expressed as a double exponential

$$n(r) = n_1 \cdot e^{-\frac{r}{\alpha_1}} + n_2 \cdot e^{-\frac{r}{\alpha_2}} \quad (4)$$

where r is geocentric distance in R_E . The zenith column brightness of Lyman α emissions that will be detected at

different altitudes, $M_C(r)$, can now be calculated by substituting $N(r)$ in equation 2 with the integral of $n(r)$ (equation 4) along the line of sight

$$M_C(r) = \sigma \cdot F \cdot \int_r^\infty (n_1 \cdot e^{-\frac{r}{\alpha_1}} + n_2 \cdot e^{-\frac{r}{\alpha_2}}) dr \quad (5)$$

which has the solution

$$M_C(r) = C_1 \cdot e^{-\frac{r}{\alpha_1}} + C_2 \cdot e^{-\frac{r}{\alpha_2}} \quad (6)$$

where

$$C_1 = \sigma \cdot F \cdot \alpha_1 \cdot n_1 \quad (7)$$

$$C_2 = \sigma \cdot F \cdot \alpha_2 \cdot n_2 \quad (8)$$

By fitting our data with a double exponential we obtain values for α_1 , α_2 , C_1 and C_2 , and n_1 and n_2 $[\text{cm}^{-3}]$ can be determined from

$$n_1 = \frac{C_1}{\sigma \cdot F \cdot \alpha_1} \quad (9)$$

$$n_2 = \frac{C_2}{\sigma \cdot F \cdot \alpha_2} \quad (10)$$

4. Data Sampling and Corrections

[13] In Figure 5 we show the calibrated, background subtracted on-axis component of the Lyman α column brightness seen by the three sensors during one spin on day 273 (September 29), 2000 from a geocentric distance of $8.12 R_E$. All three detectors are contaminated by sun-light which is indicated by the shaded regions. As the sensors are switched off when looking closer than 35° to the Sun, only the “shoulder” of the sun-light contamination is seen, which reflects the “shoulder” seen in the PSF at $\pm 80^\circ$. The dotted lines show the angle between the center line of sight and the direction to the Sun (φ_{LD}). The dashed lines show the angle between the center line of sight and local zenith (β). The angles φ_{LD} and β are illustrated in Figure A1 and defined in appendix A.

[14] From each single spin we have sampled the average Lyman α flux in 10° intervals of spin azimuth angles. This means that we from the middle sensor obtain data with β at approximately 0° , 20° , 30° etc. As the spin plane is not exactly aligned with the orbit plane, the minimum of β (middle sensor) is usually around 1° (in Figure 5 minimum β is 1.5°). In order to avoid sunlight contamination, only data when φ_{LD} (see Figure A1 in appendix A) $> 90^\circ$ are used.

[15] Measurements during solar proton events identified from GOES energetic proton data and measurements contaminated by radiation belt particles are not used.

Table 1. Geocentric Distance Where $\tau = 0.1$

Model	Geocentric Distance, R_E
<i>Rairden et al.</i> [1986]	2.8
<i>Tinsley et al.</i> [1986]	3.6
This paper for $\varphi^a = 90^\circ$	3.1
This paper for $\varphi^a = 180^\circ$	3.4

^a φ is the solar zenith angle.

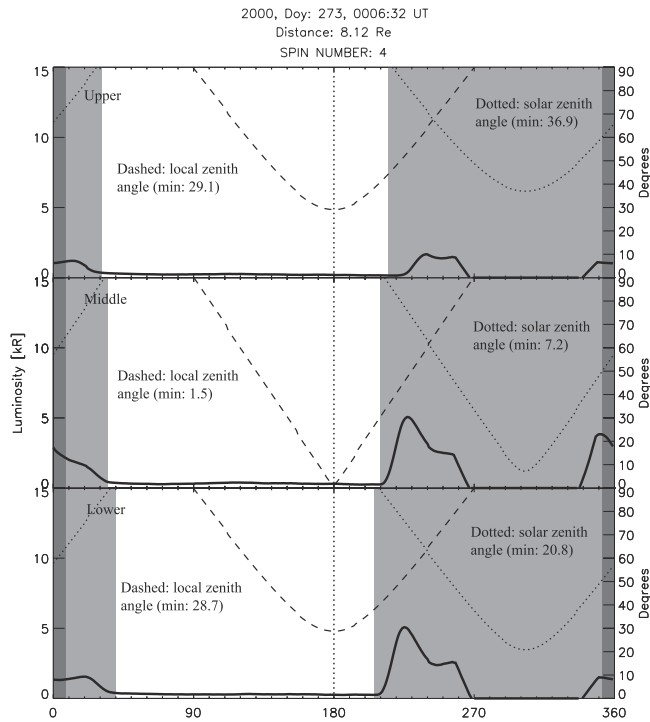


Figure 5. Lyman α brightness seen by the three sensors at 8.12 R_E on day 273, 2000 (see text for explanation).

[16] We have also excluded data when the line of sight is in the direction of the shadow of the Earth, i.e., the Earth’s “umbra”, taken to be a cylinder with radius of 1.2 R_E . As explained in Section 4.1 (and appendix A) we have also adjusted for the attenuation of the solar Lyman α flux on the night-side of the Earth and removed all data when the solar Lyman α emissions have to traverse an optical depth larger than 0.2. This implies that data from the Earth’s “penumbra” is removed as well.

[17] As our approach is based on a spherical geometry along the line of sight, we only use data when $\beta < 25^\circ$ and apply a line of sight correction when $\beta \neq 0$, as explained in appendix A. For $\beta = 25^\circ$ this correction is about 4% and for 90% of our data this correction is less than 3%. Using data when $\beta < 25^\circ$ also implies that only data from the middle sensor are used, as the two other sensors always look at $\beta > 25^\circ$. Sampling data from 338 days gives us $\sim 104,000$ data-points from the middle sensor that comply with our selection criteria. More than 100,000 of these are from altitudes above 3.5 R_E geocentric distance. To summarize, the data are from $\beta < 25^\circ$ and $\varphi = 90^\circ - 150^\circ$. The range of geocentric distances is from 2–8 R_E but only data from where the medium is optical thin ($>3.5 R_E$) can be used to obtain valid hydrogen profiles.

[18] In addition to the line of sight correction already mentioned there are a few more corrections that must be considered.

4.1. Attenuation of the Solar Lyman α Flux

[19] For observations on the night-side ($>3.5 R_E$) at solar zenith angles (φ) between $90^\circ - 150^\circ$ the solar Lyman α emissions will traverse slant paths and will be attenuated due to the optical thickness along the path. To compensate

for this attenuation each data point is adjusted by the integrated effect of this attenuation, $e^{\tau_{\text{sun}}}$, along the line of sight. τ_{sun} is the optical thickness along the solar Lyman α entering path as described in appendix A. As this adjustment is not very precise for large values of τ_{sun} we have removed data when $\tau_{\text{sun}} > 0.2$ for geocentric distances $>3.5 R_E$. This means that we have removed all data obtained from within the Earth’s “penumbra”.

4.2. Albedo From the Inner Corona

[20] The hydrogen at high altitudes is illuminated not only by the Sun but by the albedo from the inner geocorona. Although the albedo is only $<2\%$ of the solar Lyman α irradiance at 2 R_E for $\varphi > 90^\circ$, given an inner geocoronal intensity of 35 kR, the albedo contribution is subtracted from each measurements.

4.3. Phase Dependent Cross Section

[21] Owing to the anisotropic scattering phase function the solar Lyman α photons will have a preference of forward scattering resulting in slightly higher Lyman α column brightness at large solar zenith angles, even for a given spherical symmetric hydrogen distribution. In order to remove this effect from our data, we have used the scattering phase matrix from Chandrasekhar [1950, p. 51] to transform each measurement to the equivalent isotropic scattering phase function value. This adjustment is +14% for measurements at $\varphi = 90^\circ$ and -14% for measurements at $\varphi = 180^\circ$.

4.4. Attenuated Off-Axis Component From the Shadow of the Earth

[22] As the instruments PSF (Figure 4) gives us a large off-axis component (60%), a correction is applied when the Earth’s “umbra” and “penumbra” reduces this off-axis component. The procedure for this adjustment is described in appendix B. For data $>3.5 R_E$ this correction may imply an upward adjustment of as much as 10% for large solar zenith angles. However, for more than 85% of the data $>3.5 R_E$ this adjustment is less than 5%.

[23] To obtain the corrected Lyman α column brightness, M_C , referred to in Section 3, the 4 corrections described here are applied to the measured Lyman α column brightness, M_M .

$$M_C = F_4 F_3 F_2 F_1 (M_M) \quad (11)$$

where F_1 is the correction due to the attenuation of the solar Lyman α flux and when the line-of-sight is different from local zenith (equation (A9)). F_2 is the correction for the attenuated off-axis from the shadow of the Earth (equation (B9)). F_3 is the albedo correction and F_4 is the correction for the phase dependent cross section.

5. Results

[24] In Figure 6 we show the Lyman α column brightness as a function of radial distance when all the corrected data points are plotted regardless of daily variations or solar zenith angle dependence. The data gap around 3 R_E is due to radiation belt particle contamination. The solid line is a double exponential fit (equation (6)), where the parameters C_1 , C_2 , α_1 and α_2 were determined by a least squares fit to

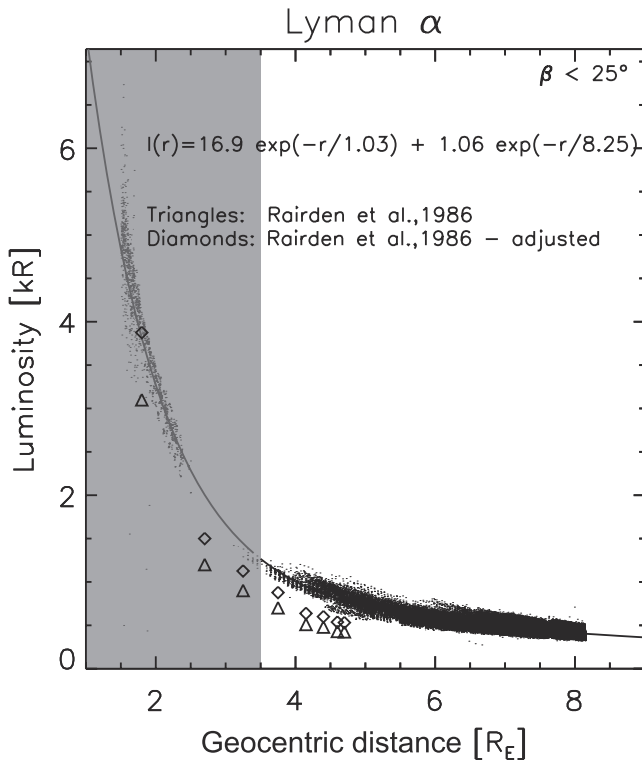


Figure 6. Profiles of Lyman α column brightness with no corrections for daily variations or solar zenith angle dependence. Solid line is the double exponential fit (equation (6)) to the data. Triangles are the values obtained by Rairden *et al.* [1986, Figure 5] and the diamonds show the same values when the 25% adjustment suggested by Woods and Rottman [1997] is applied. The shaded region indicates where the medium is considered to be optical thick ($\tau > 0.1$).

the data points using a gradient expansion algorithm [Marquardt, 1963]. Triangles show the values obtained by Rairden *et al.* [1986, Figure 5]. Diamonds show the same values when the 25% adjustment suggested by Woods and Rottman [1997] is applied. The 25% adjustment will be discussed in Section 6. The shaded region indicates where the medium is considered to be optical thick ($\tau > 0.1$).

[25] In an effort to remove some of the scatter of the data-points we have separated the daily variations from the solar zenith angle dependence. This was done by an iteration procedure. (1) First, the data were normalized to the double exponential fit. (2) The normalized data were then plotted as a function of time and the daily mean values define the 0th order approximation of the daily variation (as shown in Figure 7). (3) The normalized data were then corrected for this daily variations and then plotted as a function of solar zenith angle (φ) in each $1R_E$ interval (as shown in Figure 8). To obtain an expression for the solar zenith angle dependence we fitted the data in each $1R_E$ interval by a trigonometric function on the form

$$M(\varphi, r) = [2 + \cos(2\varphi|_r)]^\lambda \quad (12)$$

where λ was determined by a least squares fit to the data points using a gradient expansion algorithm [Marquardt, 1963]. (4) The data were then corrected for both the daily variation (from step 2) and the solar zenith angle dependence above $3.5 R_E$ (equation (12), from step 3) to get the yearly average of Lyman α column brightness at $\varphi = 90^\circ$, which gives us a better estimate of the double exponential fit. This procedure (1–4) was repeated until both the daily variation, the solar zenith angle dependence and the double exponential fit converged. The final daily variation for normalized data (when solar zenith angle dependence was removed) is shown in Figure 7 and the final solar zenith angle

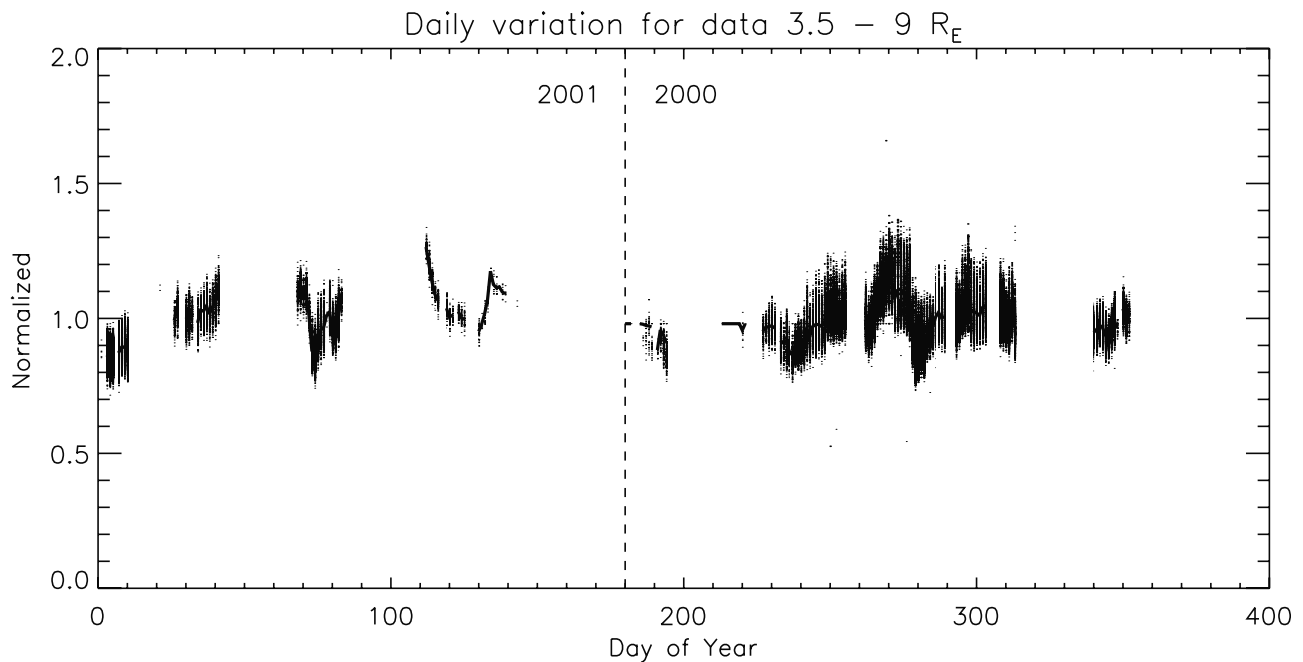


Figure 7. Daily variation of the normalized Lyman α column brightness ($>3.5 R_E$) when solar zenith dependence is removed. Solid line shows the average values.

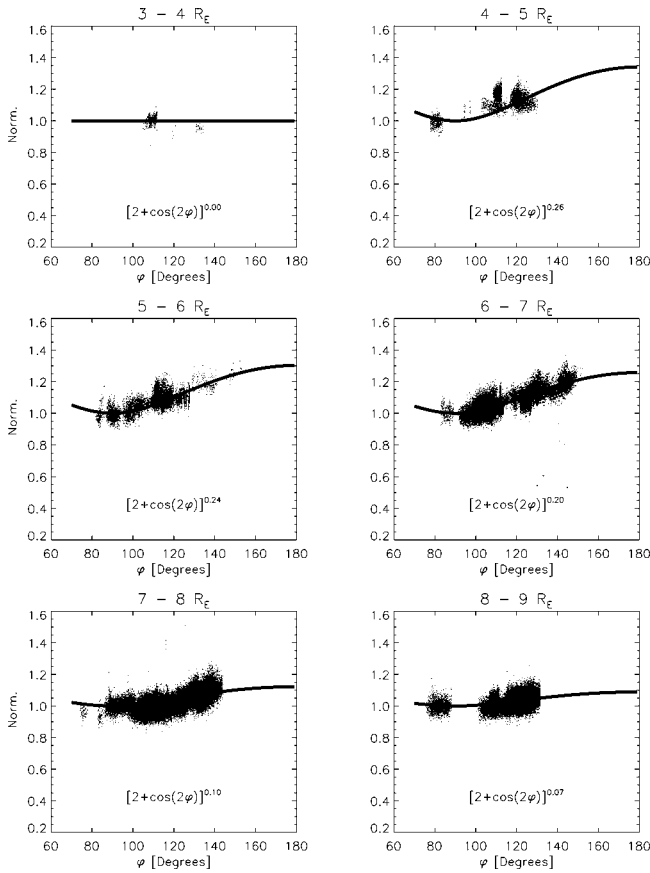


Figure 8. Solar zenith dependence at different geocentric distances of the normalized Lyman α column brightness when the daily variation is removed. Solid lines show the trigonometric fits (equation (12)) to the data.

dependence for normalized data (when daily variations were removed) is shown in Figure 8.

[26] In Figure 9 we show the yearly average of Lyman α column brightness profile at $\varphi = 90^\circ$, i.e., when both daily variation and solar zenith dependence above $3.5 R_E$ are removed. The scatter from Figure 6 is reduced by a factor of ~ 2 . In Figure 10 we show the yearly average hydrogen density profile at $\varphi = 90^\circ$ using the method described in Section 3. The vertical error bars account for the calibration uncertainty (Section 2.4), the $1\text{-}\sigma$ uncertainty of the solar Lyman α flux (Section 2.2) and the uncertainties due to counting statistics. Triangles show the values obtained by *Rairden et al.* [1986] (October 14, 1981, their Figure 6) and diamonds show the same values when the 25% adjustment suggested by *Woods and Rottman* [1997] is applied (see Section 6). Crosses show the values presented by *Tinsley et al.* [1986] for solar maximum condition, which corresponds to the conditions for the model by *Rairden et al.* [1986] and this study. The squares show the solstice values from *Hodges* [1994] for F10.7 = 180, which corresponds to the average F10.7 value for the time interval examined in this study.

6. Discussion

[27] By normalizing the Lyman α column brightness by daily variations and solar zenith angle dependence a signifi-

cant part of the scatter in the data has been removed. On the other hand, the daily variations as well as the solar zenith angle variations are only slightly larger than the uncertainties of our model. However, most of the 30% model uncertainty stems from the calibration of the instrument (25%) and represents a systematic error. The errors due to the solar Lyman α flux (5%) and counting statistics ($<5\%$) are still smaller than both the daily variations ($\pm 20\%$) and the solar zenith angle variations ($>30\%$). We therefore interpret our result as an indication that the hydrogen density in the night side of the Earth is cylindrical symmetric about the Earth-Sun line and varies with time. The daily variation is not due to any instrumental effects. We have examined solar Lyman α data, the EUV data from SEM/SOHO in the 26–34 nm range (covers the He II 30.4 nm emission) and 0.1–50 nm range as well as the F10.7 emission (data not shown) without finding any significant correlation with solar quantities. The daily variations do not show any direct correlation with the Dst index either.

[28] Our Lyman α column brightness profiles show a solar zenith dependence at geocentric distances from $4 R_E$ to $7 R_E$ (Figure 8). This can be explained by solar Lyman α radiative pressure [*Bishop, 1985; Tinsley et al., 1986*], which will give the satellite neutral hydrogen atoms slightly elliptic orbits resulting in enhanced hydrogen density in the

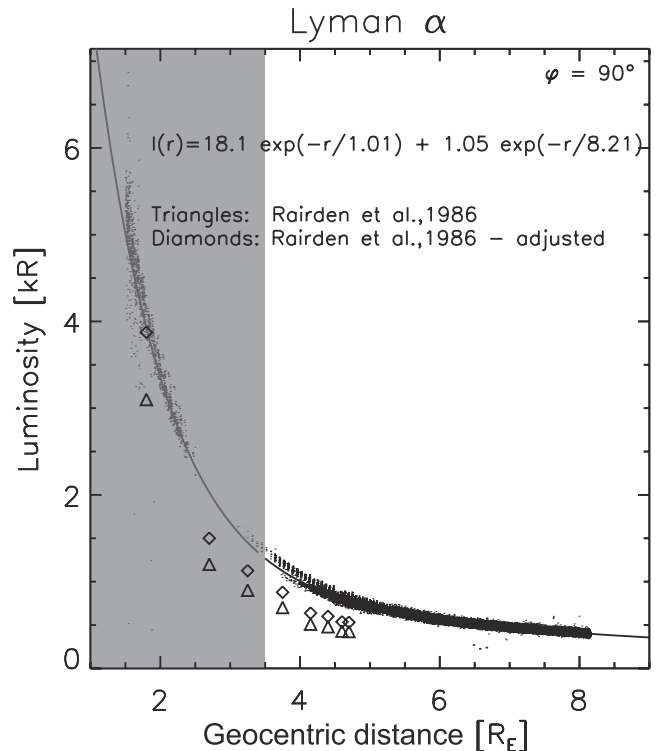


Figure 9. Yearly average of Lyman α column brightness profile at $\varphi = 90^\circ$ when both daily variation and solar zenith dependence above $3.5 R_E$ are removed. Solid line is the double exponential fit (equation (6)) to the data. Triangles are the values obtained by *Rairden et al.* [1986] and the diamonds show the same values when the 25% adjustment suggested by *Woods and Rottman* [1997] is applied. The shaded region indicates where the medium is considered to be optical thick ($\tau > 0.1$).

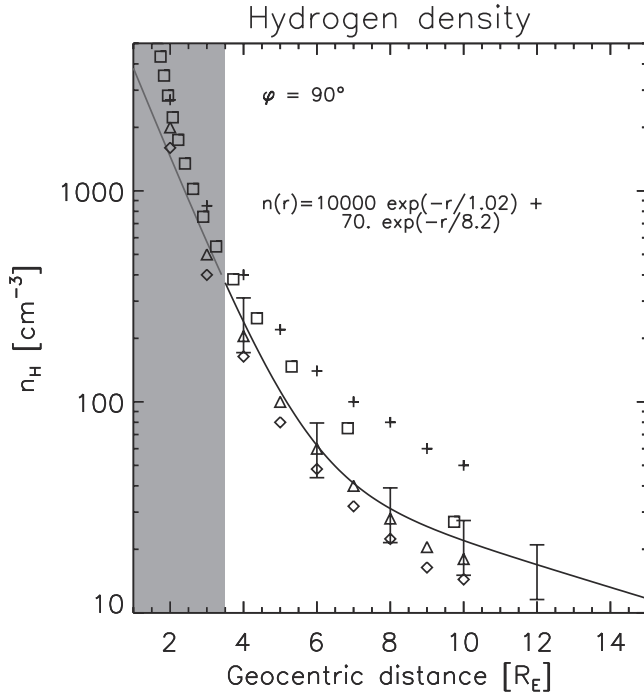


Figure 10. Yearly average hydrogen density profile at $\varphi = 90^\circ$. Triangles (diamonds) show the values (adjusted values) obtained by *Rairden et al.* [1986]. Crosses show the values obtained by *Tinsley et al.* [1986] for solar maximum condition. Squares show solstice values from *Hodges* [1994] for average solar maximum conditions. Solid line is the hydrogen density profile we derive using the values from the double exponential fit in Figure 9 as input to equations (9) and (10). The vertical error bars account for the calibration uncertainty, the 1- σ uncertainty of the solar Lyman α flux and uncertainties due to counting statistics. The shaded region indicates where the medium is considered to be optical thick ($\tau > 0.1$).

night-side of the Earth. The existence of this feature, referred to as a geotail in the literature, was first reported by *Thomas and Bohlin* [1972] and confirmed by *Rairden et al.* [1986]. Our data support the existence of a geotail.

[29] To obtain hydrogen density profiles in 10° solar zenith angle intervals we use the yearly average Lyman α profile at $\varphi = 90^\circ$ (Figure 9) and adjust for solar zenith angle dependence (equation (12)) above $3.5 R_E$. The results are presented in Figure 11 showing increasing hydrogen density above $4 R_E$ for each 10° solar zenith angle interval from $\varphi = 90^\circ$ (lower profile) to $\varphi = 180^\circ$ (upper profile). Our hydrogen density model can now be expressed as

$$n(r, t, \varphi) = C(t) \left[n_1(\varphi) e^{-\frac{r}{\alpha_1(\varphi)}} + n_2(\varphi) e^{-\frac{r}{\alpha_2(\varphi)}} \right] \quad (13)$$

where r is given in R_E and the parameters n_1 , α_1 , n_2 and α_2 for different solar zenith angles (φ) are listed in Table 2.

[30] $C(t)$ is determined empirically from Figure 7 and is a constant for a specific day. $C(t)$ varies between 0.8 and 1.3. As discussed above this is larger than the uncertainties due to the uncertainties in the solar Lyman α flux and the counting statistics. We therefore believe that the temporal

variations are real. We emphasize that our results are only valid above $3.5 R_E$ as indicated by the shaded region in Figures 10 and 11.

[31] Figures 6 and 9 show that the data can be fitted fairly well with a double exponential function. As described in Section 3, this implies that the hydrogen density also can be expressed as a double exponential. It is interesting to notice that this functional form replicates the two-temperature model that has been frequently used to analyze the hydrogen density on Venus [*Takacs et al.*, 1980; *Bertaux et al.*, 1982; *Paxton and Anderson*, 1992]. According to *Paxton and Anderson* [1992] such a two-component density profile also exists in the exospheres of Mars and Earth, but is hard to observe due to the large scale heights of thermal hydrogen on these two planets. They postulate that measurements must be obtained from high in the exosphere during low solar activity to be able to observe the two-component density profile. Although our measurements are obtained during solar maximum they are definitely from high in the exosphere and they do indeed indicate a two-component hydrogen density profile.

[32] In Figures 6, 9, 10, and 11 we have shown both the original and the adjusted results from *Rairden et al.* [1986]. The downward adjustment was suggested by *Woods and Rottman* [1997] as they claimed that *Rairden et al.* [1986] used too low values for the solar Lyman α fluxes. *Rairden*

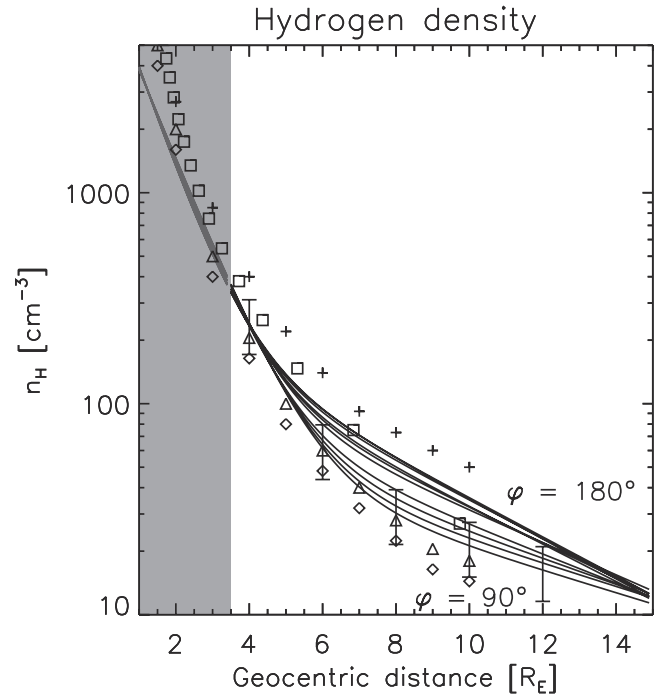


Figure 11. Solid lines show the yearly average hydrogen density profiles from $\varphi = 90^\circ$ (lower profile) to $\varphi = 180^\circ$ (upper profile) using equation (13) with the values listed in Table 2. As in Figure 10 triangles (diamonds) show the values (adjusted values) obtained by *Rairden et al.* [1986]. Crosses show the values obtained by *Tinsley et al.* [1986] for solar maximum condition. Squares show solstice values from *Hodges* [1994] for average solar maximum conditions. The shaded region indicates where the medium is considered to be optical thick ($\tau > 0.1$).

Table 2. Hydrogen Density Parameters for Equation (13)

φ^a	n_1, cm^{-3}	α_1, R_E	n_2, cm^{-3}	α_2, R_E
90	10000	1.02	70	8.2
100	10100	1.01	80	7.9
110	10300	0.99	100	7.1
120	10600	0.96	130	6.3
130	10900	0.93	180	5.7
140	11300	0.90	220	5.2
150	11600	0.88	250	4.9
160	11800	0.86	280	4.8
170	12000	0.85	300	4.7
180	12000	0.85	310	4.6

^a φ is the solar zenith angle.

et al. [1986] used the solar Lyman α flux from the Solar Mesosphere Explorer (SME). Comparing the measurements from UARS and SME over 2 solar cycles *Woods and Rottman* [1997] found that the SME Lyman α irradiances should be adjusted up by 25%. An underestimate of the solar Lyman α flux will lead to an overestimate of hydrogen density and the hydrogen density profiles from *Rairden et al.* [1986] should be adjusted down by a factor of 1/1.25. The corrected values are shown by diamonds. However, our lowest profile ($\varphi = 90^\circ$) is almost identical with the original results from *Rairden et al.* [1986] (triangles) from 3.5–8 R_E . Above $\sim 8 R_E$ we derive slightly higher densities than *Rairden et al.* [1986]. Our result for $\varphi = 90^\circ$ (Figure 10) show densities lower (about a factor of 2) than the profile presented by *Tinsley et al.* [1986] and slightly lower than the profile presented by *Hodges* [1994]. For larger solar zenith angles (Figure 11) our results are closer to both these models and show densities significantly higher than the results from *Rairden et al.* [1986].

[33] The data presented by *Rairden et al.* [1986] showed enhanced Lyman α column brightness from the night-side of the Earth. Our results support the existence of a geotail and show a $\sim 40\text{--}50\%$ increase in hydrogen density for $\varphi = 180^\circ$ (compared to $\varphi = 90^\circ$) between 6 R_E and 12 R_E . Above 3.5 R_E our result indicates an excess of $\sim 0.5 \cdot 10^{11}$ [atoms cm^{-2}] at $\varphi = 180^\circ$ compared to $\varphi = 90^\circ$ solar zenith angle, which is slightly lower than the $2 \cdot 10^{11}$ [atoms cm^{-2}] geotail column density in excess of the *dayside* ($\varphi = 0$) column density estimated by *Bishop* [1985].

[34] Contrary to some earlier reports [e.g., *Wallace et al.*, 1970; *Bertaux and Blamont*, 1973] we do not find any evidence for depletion due to charge exchange with solar wind protons at high altitudes. During disturbed times when the magnetopause is compressed the IMAGE satellite can spend hours outside the magnetopause, but the Lyman α column brightness at local zenith does not show signatures of such hydrogen depletion. This is in agreement with the final results from DE 1 [*Rairden et al.*, 1986] who found that the satellite population was not depleted as severely at high altitudes as these earlier investigations suggested. However, the time constant for solar ionization loss may be of the order of days (16 days suggested by *Bishop* [1991]) and consequently not observable for time-spans of hours.

[35] As mentioned in section 2.3 there may be a systematic error to our results stemming from the uncertainties in the background model [*Pryor et al.*, 1998a] we have used. If the background should be a factor 2 higher, our Lyman α

profile should be lower, giving an even lower hydrogen density profile. On the other hand, an underestimate of the background by a factor of 2 would imply an unreasonable high hydrogen density at e.g., 12 R_E . Although background errors by a factor of 2 seem unlikely, we should emphasize that our results certainly depend on the accuracy of the background model we have applied.

7. Conclusions

[36] The geocoronal imaging data from GEO on IMAGE have been used to present an empirical model of the hydrogen density at high altitudes on the night-side of the Earth that shows the following features.

[37] (1) The hydrogen density is cylindrical symmetric around the Sun-Earth line with an enhanced density at large solar zenith angles, the so-called geotail.

[38] (2) The hydrogen density shows temporal variations in the range of $\pm 20\%$ which is not controlled by any solar quantity or geomagnetic parameter alone.

[39] (3) Our lowest hydrogen density profile ($\varphi = 90^\circ$) shows densities similar to what was reported by *Rairden et al.* [1986]. Above 8 R_E our model indicates higher densities than *Rairden et al.* [1986].

[40] (4) The yearly average profile can be expressed as a double exponential with a $\sim 40\text{--}50\%$ increase in the geotail between 6 R_E and 12 R_E . Tabulated values to be used as input in a double exponential function are presented for solar zenith angles from $\varphi = 90^\circ$ to $\varphi = 180^\circ$. A constant can be applied to get the profile for a specific day.

[41] (5) Our results are only valid above 3.5 R_E .

Appendix A: Solar Lyman α Attenuation and Line of Sight Correction

[42] The correction due to the attenuation of the solar Lyman α flux and the correction needed when the line of sight is not at local zenith are essentially the same kind of corrections, as they both are functions of optical thickness and require an assumption about the hydrogen density profile. We start with the solar Lyman α attenuation.

[43] As shown in Figure A1 the solar Lyman α beam is entering (from the left) along r_S and is attenuated along the path from the Sun to (r_{SC}, φ_{SC}) giving the effective solar Lyman α , F_E , at location (r_{SC}, φ_{SC})

$$F_E(r_{SC}, \varphi_{SC}) = F \cdot e^{-\tau_{\text{sun}}(r_{SC}, \varphi_{SC})} \quad (\text{A1})$$

F is the incident solar Lyman α flux (defined in equation (3)) and τ_{sun} is the optical thickness for solar Lyman α at (r_{SC}, φ_{SC})

$$\tau_{\text{sun}}(r_{SC}, \varphi_{SC}) = \sigma \cdot N(r_{SC}, \varphi_{SC}) \quad (\text{A2})$$

$N(r_{SC}, \varphi_{SC})$ is the column density of hydrogen along r_S to (r_{SC}, φ_{SC}) . The optical thickness, τ_{sun} , along the path r_S at (r_{SC}, φ_{SC}) is, according to *Rees* [1989, p.13], given by

$$\tau_{\text{sun}}(r_{SC}, \varphi_{SC}) = 2\sigma \int_{r_{\text{sn}}}^{\infty} n(r) \left[1 - \left(\frac{r_{\text{sn}}}{r} \right)^2 \right]^{-1/2} dr - \sigma \int_{r_{\text{sc}}}^{\infty} n(r) \left[1 - \left(\frac{r_{\text{sc}}}{r} \right)^2 \sin^2(\varphi_{\text{sc}}) \right]^{-1/2} dr \quad (\text{A3})$$

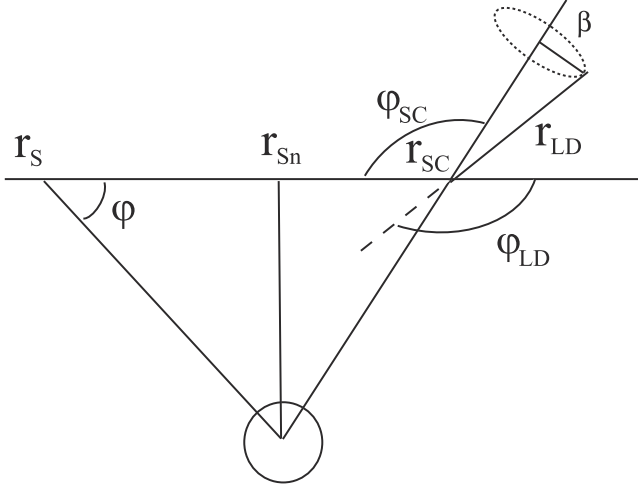


Figure A1. The geometry for the solar Lyman α attenuation and the line of sight correction. The symbols are explained in the text.

where r_{SC} is the spacecraft location and φ_{SC} is the spacecraft solar zenith angle. The effective solar Lyman α flux at (r_{SC} , φ_{SC}) is given by equation (A1).

[44] We define β to be the local zenith angle, i.e., the angle between the look direction (r_{LD}) and the spacecraft vector (r_{SC}). An estimate of a measurement, M_E , from (r_{SC} , φ_{SC}) along β (local zenith angle) can then be expressed as

$$M_E(r_{SC}, \varphi_{SC}, \beta) = \int_{r_{SC}}^{\infty} \sigma \cdot F \cdot e^{-\tau_{\text{sun}}(r, \varphi_{SC})} \frac{n(r, \beta)}{\cos(\beta)} dr \quad (\text{A4})$$

We have then assumed that the difference in attenuated solar Lyman α fluxes along φ_{LD} and φ_{SC} (from r_{SC}) is very small. φ_{LD} is the look direction solar zenith angle. Similar can an estimated measurement along φ_{SC} ($\beta = 0^\circ$) be expressed

$$M_E(r_{SC}, \varphi_{SC}, 0) = \int_{r_{SC}}^{\infty} \sigma \cdot F \cdot e^{-\tau_{\text{sun}}(r, \varphi_{SC})} n(r, 0) dr \quad (\text{A5})$$

To transform the measurement along β to the equivalent measurement along φ_{SC} ($\beta = 0$) our measurement can be multiplied by the line-of-sight correction factor

$$C_{LOS} = \frac{M_E(r_{SC}, \varphi_{SC}, 0)}{M_E(r_{SC}, \varphi_{SC}, \beta)} \quad (\text{A6})$$

An estimate of what we would measure at r_{SC} along φ_{SC} if the solar Lyman α flux was not attenuated along r_S is given by

$$M_{EC}(r_{SC}, \varphi_{SC}, 0) = \int_{r_{SC}}^{\infty} \sigma \cdot F \cdot n(r, 0) dr \quad (\text{A7})$$

which gives the correction factor

$$C_A = \frac{M_{EC}(r_{SC}, \varphi_{SC}, 0)}{M_E(r_{SC}, \varphi_{SC}, 0)} \quad (\text{A8})$$

Each measurement can now be corrected for the solar Lyman α attenuation and the line-of-sight different from local zenith by

$$M_C(r_{SC}, \varphi_{SC}) = C_{LOS} \cdot C_A \cdot M(r_{SC}, \varphi_{SC}, \beta) \quad (\text{A9})$$

[45] In order to run through the entire scheme of deriving the hydrogen profile we need an initial hydrogen profile to perform the first corrections. For this purpose we use the density profile obtained by *Rairden et al.* [1986]. Then we plug in the density profile from our own deriving scheme and repeat the entire procedure until the derived hydrogen density profile converge.

Appendix B: Correction When Part of the Off-Axis Component is From the Earth's "Umbra" and "Penumbra"

[46] As our measurements have a large off-axis component, our signal will be decreased when a large part of the off-axis component comes from the Earth's "umbra", which we define as a cylinder with a radius of $1.2 R_E$. In addition to this there will be a "penumbra" where the solar Lyman α fluxes are largely attenuated due to the optical depth the emissions have to traverse. We define the "penumbra" to extend to where the solar Lyman α is reduced by $1/e$ and then consider the "penumbra" to be an area where the solar Lyman α flux on average is reduced by a factor of 2. On the basis of the τ_{sun} values appendix A the "penumbra" is a cylinder with radius $1.7 R_E$.

[47] Referring to Figure B1 we first define the angle θ_{LD} which is complementary to the look direction solar zenith angle, φ_{LD}

$$\theta_{LD} = 180^\circ - \varphi_{LD} \quad (\text{B1})$$

r_2 can then be expressed as

$$r_2 = \frac{r_{SC} \cdot \sin \theta_{LD}}{\cos(\theta_{LD} - \gamma)} \quad (\text{B2})$$

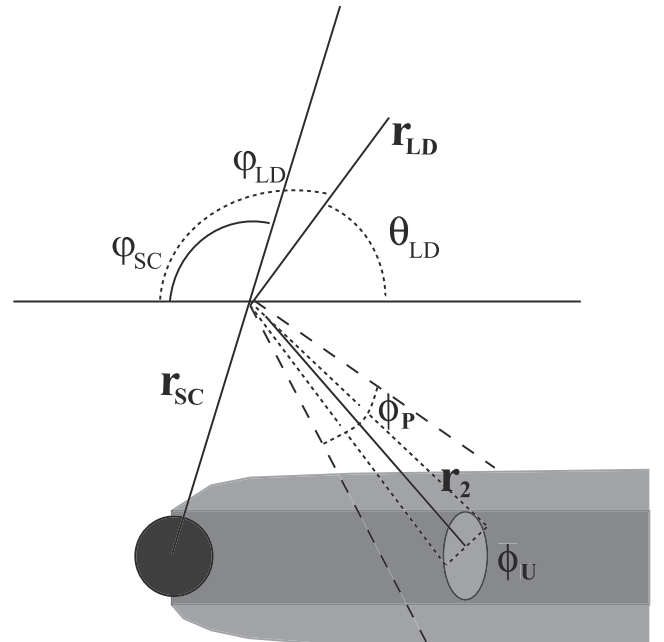


Figure B1. The geometry for correction needed when the off-axis component has a contribution from the Earth's "umbra" and "penumbra". The symbols are explained in the text.

where γ is defined as

$$\gamma = \varphi_{LD} - \varphi_{SC} \quad (B3)$$

[48] The azimuthal extension, ϕ , of the Earth's "umbra" as seen in the $\pm 90^\circ$ FOV (off-axis component) is related to r_2 as

$$\phi_U = 2 \cdot \sin^{-1} \left(\frac{1.2}{r_2} \right) \quad (B4)$$

and similar for the "penumbra"

$$\phi_P = 2 \cdot \sin^{-1} \left(\frac{1.7}{r_2} \right) \quad (B5)$$

If our signal was not attenuated by any shadow the response would be

$$total = 2\pi \int_0^{\pi/2} PSF(\theta) \sin(\theta) d\theta \quad (B6)$$

where $PSF(\theta)$ is the Point Spread Function. The attenuated signal from the "umbra" and "penumbra" is given by

$$\sigma = (\phi_U + 0.5\phi_P) \int_{\theta_{LD}}^{\pi/2} PSF(\theta) \sin(\theta) d\theta \quad (B7)$$

and our correction factor, C_{UP} , is given by

$$C_{UP} = \frac{total}{total - \sigma} \quad (B8)$$

The corrected data are given by

$$M_C(r_{SC}, \varphi_{SC}, \varphi_{LD}) = C_{UP} \cdot M(r_{SC}, \varphi_{SC}, \varphi_{LD}) \quad (B9)$$

[49] **Acknowledgments.** The IMAGE FUV investigations were supported by NASA through SwRI subcontract number 83820 at the University of California at Berkeley under contract number NAS5-96020. We acknowledge Wayne Pryor for providing the interplanetary and local interstellar medium Lyman α fluxes and the UARS/SOLSTICE team for providing the solar Lyman α data.

[50] The Editor thanks Brian Tinsley and another reviewer for their assistance in evaluating this manuscript.

References

- Anderson, D. E., Jr., and C. W. Hord, Multidimensional radiative transfer applications to planetary coronae, *Planet. Space Sci.*, 25, 563–571, 1977.
- Anderson, D. E., Jr., R. R. Meier, R. R. Hodges, and B. A. Tinsley, Hydrogen Balmer alpha intensity distribution and line profiles from multiple scattering theory using realistic geocoronal models, *J. Geophys. Res.*, 92, 7619, 1987.
- Bertaux, J. L., and J. E. Blamont, Interpretation of OGO 5 Lyman alpha measurements in the upper geocorona, *J. Geophys. Res.*, 78, 80–91, 1973.
- Bertaux, J.-L., V. M. Lepine, V. G. Kurt, and A. Smirnov, Altitude profile of H in the atmosphere of Venus from Lyman α observations of Venera 11 and Venera 12 and origin of the hot exospheric component, *Icarus*, 52, 221–244, 1982.
- Bertaux, J.-L., H. Le Texier, F. Goutail, R. Lallement, and G. Kockarts, Lyman alpha observations of geocoronal and interplanetary hydrogen from Spacelab-1: Exospheric temperature and density and hot emission, *Ann. Geophys.*, 7, 549–564, 1989.
- Bishop, J., Geocoronal structure: The effect of solar radiation pressure and plasmasphere interaction, *J. Geophys. Res.*, 90, 5235–5245, 1985.
- Bishop, J., Analytic exosphere models for geocoronal applications, *Planet. Space Sci.*, 39, 885–893, 1991.
- Bishop, J., Transport of resonant atomic hydrogen emissions in the thermosphere and geocorona: Model description and applications, *J. Quant. Spectrosc. Radiat. Transfer*, 61, 473–491, 1999.
- Chamberlain, J. W., Planetary coronae and atmospheric evaporation, *Planet. Space Sci.*, 11, 901–960, 1963.
- Chandrasekhar, S., The equation of transfer, *Radiative Treansfer*, pp. 50–52, Clarendon Press, Oxford, England, 1950.
- Donahue, T. M., The problem of atomic hydrogen, *Ann. Geophys.*, 22, 175–188, 1966.
- Fok, M. C., T. E. Moore, J. U. Kozyra, G. C. Ho, and D. C. L. Hamilton, 3-dimensional ring current decay model, *J. Geophys. Res.*, 100, 9619–9632, 1995.
- Hedin, A. E., Extension of the MSIS thermosphere model into the middle and lower atmosphere, *J. Geophys. Res.*, 96, 1159–1172, 1991.
- Hodges, R. R., Monte Carlo simulation of the terrestrial hydrogen exosphere, *J. Geophys. Res.*, 99, 23,229–23,247, 1994.
- Kistler, L. M., F. M. Ipavich, D. C. Hamilton, G. Gloeckler, B. Wilken, G. Kremser, and W. Stüdemann, Energy spectra of the major ion species in the ring current during geomagnetic storms, *J. Geophys. Res.*, 94, 3579–3599, 1989.
- Kupperian, J. E., Jr., E. T. Byram, T. A. Chubb, and H. Friedman, Far ultraviolet radiation in the night sky, *Planet. Space Sci.*, 1, 3–6, 1959.
- Marquardt, D. W., An algorithm for least-squares estimation of nonlinear parameters, *J. Soc. Ind. Appl. Math.*, 11, 431–441, 1963.
- Mende, S. B., et al., ultraviolet imaging from the IMAGE spacecraft: 3. Spectral imaging of Lyman- α and OI 135.6 nm, *Space Sci. Rev.*, 191, 287–318, 2000.
- Paxton, L. J., and D. E. Anderson, Far ultraviolet remote sensing of Venus and Mars, in *Venus and Mars: Atmospheres, ionospheres, and solar wind interactions*, *Geophys. Monogr. Ser.*, vol. 66, edited by J. G. Luhmann and M. Tatrallyay, pp. 113–189, AGU, Washington, D.C., 1992.
- Pryor, W. R., et al., Latitude variations in interplanetary Lyman α from the Galileo EUVS modeled with solar He 1083 nm images, *Geophys. Res. Lett.*, 23, 1893–1896, 1996.
- Pryor, W. R., S. J. Lasicca, A. I. F. Stewart, D. T. Hall, S. Lineaweaver, W. B. Colwell, J. M. Ajello, O. R. White, and W. K. Tobiska, Interplanetary Lyman α observations from Pioneer Venus over a solar cycle from 1978 to 1992, *J. Geophys. Res.*, 103, 26,833–26,849, 1998a.
- Pryor, W. R., M. Witte, and J. M. Ajello, Interplanetary Lyman α remote sensing with the Ulysses Interstellar Natural Gas Experiment, *J. Geophys. Res.*, 103, 26,813–26,831, 1998b.
- Rairden, R. L., L. A. Frank, and J. D. Craven, Geocoronal imaging with Dynamics Explorer, *J. Geophys. Res.*, 91, 13,613–13,630, 1986.
- Rees, M. H., *Physics and Chemistry of the Upper Atmosphere*, Cambridge Univ. Press, New York, 1989.
- Takacs, P. Z., A. L. Broadfoot, G. R. Smith, and S. Kumar, Mariner 10 observations of hydrogen Lyman alpha emission from the Venus exosphere: Evidence of complex structure, *Planet. Space Sci.*, 28, 687–701, 1980.
- Thomas, G. E., and R. C. Bohlin, Lyman-alpha measurements of neutral hydrogen in the outer geocorona and in interplanetary space, *J. Geophys. Res.*, 77, 2752–2761, 1972.
- Tinsley, B. A., R. R. Hodges Jr., and R. P. Rhorbaugh, Monte carlo models for the terrestrial exosphere over a solar cycle, *J. Geophys. Res.*, 91, 13,631–13,647, 1986.
- Wallace, L., C. A. Barth, J. B. Pearce, K. K. Kelly, D. E. Anderson Jr., and W. G. Fastie, Mariner 5 measurements of the Earth's Lyman alpha emission, *J. Geophys. Res.*, 75, 3769–3777, 1970.
- Woods, T. N., and G. J. Rottman, Solar Lyman alpha irradiance measurements during two solar cycles, *J. Geophys. Res.*, 102, 8769–8779, 1997.
- Woods, T., N. Tobiska, W. K. Rottman, and G. J. Worden, Improved solar Lyman alpha irradiance modeling from 1947 to 1999 based on UARS observations, *J. Geophys. Res.*, 105, 27,195–27,216, 2000.

H. U. Frey, S. B. Mende, and N. Østgaard, Space Sciences Laboratory, University of California, Berkeley, California, CA 94720, USA. (nikost@ssl.berkeley.edu)

G. R. Gladstone, Southwest Research Institute, 6220 Culebra Road, San Antonio, Texas, TX 78238, USA.

H. Lauche, Max Planck Institute for Aeronomy, D-37189 Katlenburg-Lindau, Germany.